An Experimental Study of Nonisothermal Effectiveness Factors in a Porous Catalyst

F. W. MILLER and H. A. DEANS

Rice University, Houston, Texas

Circulating hydrogen-oxygen mixtures were reacted at atmospheric pressure in a single long porous catalyst cylinder which contained a thermocouple-micromanometer probe. Rate and temperature rise data were obtained at 20°, 30°, 50°, and 60°C. in the concentration range 0 to 5% oxygen in hydrogen.

The data were used in connection with the transport equations to obtain effectiveness factors, rate constant, activation energy, and reaction order for oxygen concentration.

The necessity of considering thermal effects is exhibited clearly by this system. The maximum temperature rise observed inside the catalyst (33°C.) is associated with a 60% increase in utilization factor over the isothermal value.

The heat and mass transfer steps which accompany chemical reactions occurring in porous catalyst pellets have received considerable attention in recent years. Much of the published work has been concerned with isothermal systems, specifically with the experimental evaluation and theoretical prediction of effective diffusion coefficients and utilization (effectiveness) factors. A review of literature on this subject is given by Petersen (*10*).

Theoretical consideration of nonisothermal cases has been the subject of several recent papers (*2, 7, 18*). This work was undertaken to test the proposed theory, and had the following specific objectives:

1. To determine experimentally the overall rate of an exothermic reaction occurring in a long porous catalyst cylinder and to measure concurrently the temperature and pressure differences between the center and surface of the catalyst cylinder.
2. To measure the effective thermal conductivity and effective diffusion coefficient for the catalyst pellets under conditions as similar as possible to those under which the rate data were taken.
3. To calculate theoretical temperature profiles and effectiveness factors for the catalyst and to compare them with the experimental observations and isothermal predictions.†

The hydrogen-oxygen-water reaction system was chosen for its high heat of reaction and relatively large molecular diffusion coefficients. Platinized alumina cylinders, furnished by Engelhard Industries, were used as received to construct the catalyst assembly. Relatively low thermal conductivity, high catalytic activity at low temperature, and high porosity were desirable properties possessed by this material.

The phenomena of interest were observed under steady state conditions in the range 0 to 5% oxygen in hydrogen, 20° to 60°C., and approximately 1 atm. total system pressure. Upper and lower temperature limits were set by bath design and rate measurement inaccuracies, respectively. The upper limit on oxygen concentration was approximately the lower explosion limit; oxygen-rich mixtures above the upper explosion limit were not investigated.

EXPERIMENTAL APPARATUS AND PROCEDURE

Catalyst Assembly

The long ($L = 5D$) catalyst cylinders shown in Figure 1 consisted of five 3/8-in. × 3/8-in. cylindrical pellets glued end to end. The catalytically active pellets were molded from microporous granules of 0.05% by weight platinum on alumina support. The blank pellets were nominally identical except for the absence of platinum. Blank runs proved the latter to be inactive catalytically within the limits of experimental error.

Both active and blank pellets had measured (*6*) bulk density of 1.34 g./cc., surface area of about 60 sq. meters/g., and accessible void fraction of 0.50. The latter was divided into 0.35 macrovoid fraction (pore size above 120 Å.) and 0.15

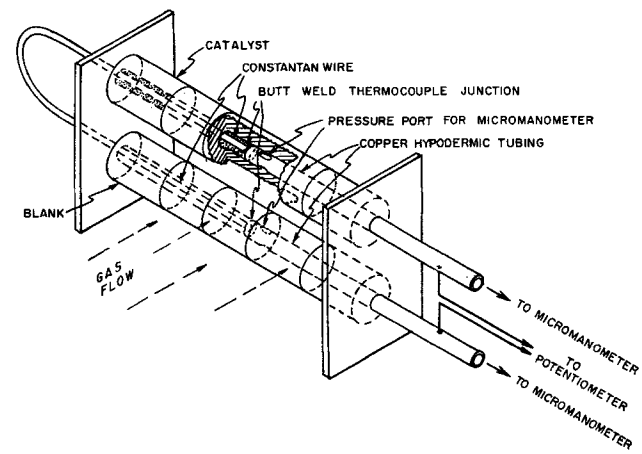

Fig. 1. Catalyst assembly.

† During final revision of this paper, one of the authors had the opportunity to review very similar experimental work by Maymo and Smith (*5*). The agreement of the results reported here with those of the latter authors is good.

F. W. Miller is at E. I. du Pont de Nemours and Company, Inc., Wilmington, Delaware.

microvoid fraction (pore size below 120 Å.). Pore size distribution measurements, obtained by the mercury penetration method, indicated a peak near 900 Å. This value was used later in correcting thermal conductivity measurements.

The pellets were drilled axially and mounted on the thermocouple-micromanometer probe and then were glued, as indicated in Figure 1. The pellet cylinders were compressed between a smaller and a larger (flange) end plate by four springs. The entire assembly was mounted and sealed in the flow apparatus by means of the flange. The gas flow was such that the active and blank cylinders were in hydrodynamically similar positions to avoid flow-induced pressure differences across the micromanometer.

Both the 0.023-in. O.D. copper hypodermic tubing and the 28-gauge constantan wire, which completed the differential thermocouple, were glued into the axial holes to avoid leakage from the center of the pellets along the axis. The hypodermic tubes were connected to an inclined tube manometer with nonconducting tubing to avoid shorting the thermocouple circuit. The potential across the differential thermocouple was determined with a Leeds and Northrup Model 8686 potentiometer.

Gas Circulation System

The reaction gas mixture was circulated over the catalyst assembly by the closed-loop flow system shown in Figure 2. A continuous flow rate of up to 15 cu. ft./min. was provided by a two-cylinder opposed diaphragm type of pump (*6*). The pump was designed to produce less than 10% pulsation in output rate, which was further smoothed by external system capacity and flow resistance. The flow was regulated within the desired limits with a by-pass. The gas velocity was measured by a Pitot tube mounted directly behind the center of the catalyst-blank assembly.

The temperature of the reaction gas was controlled within $\pm$ 0.5°C. by the bath, which was used mainly to remove the heat generated by pumping. All lines beyond the bath were insulated, and the rate of heat generation by the reaction was completely negligible for the flow rates used. The water produced during a run was collected on silica gel in two driers mounted in parallel. Flow was directed through one of the driers during start-up of a run. After steady conditions were reached, flow was switched to the second drier which had been dried and weighed on a 10-kg. capacity Sauter analytical balance. The balance had a sensitivity of about 2 mg.; runs were therefore continued until at least 200 mg. of water had been produced and collected.

Since the product water was removed quantitatively as it was formed, the pressure in the flow system had to be maintained by continuous make-up of hydrogen and oxygen. The reactants were replaced in stoichiometric proportion by a water electrolysis cell, so that gas phase composition remained essentially constant during a run. Current to the cell was controlled by a circuit actuated by contacts in the system mercury manometer. Average electrolysis cell current was a secondary measure of reaction rate.

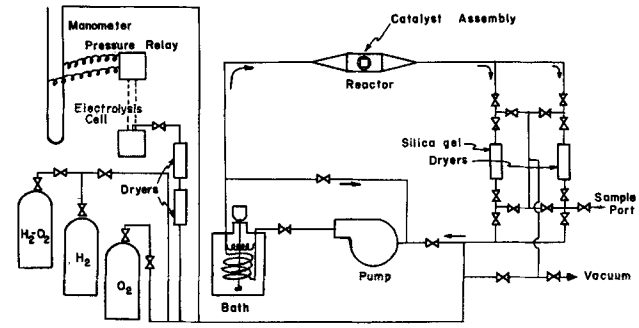

Fig. 2. Schematic diagram of the gas circulation system.

Reaction Rate Runs

The flow system was evacuated and filled with reaction mixture of approximately the desired composition. Circulation was begun with the spare dryer on line and continued until bulk gas temperature, system pressure, catalyst-blank center temperature difference, and electrolysis cell output were stable. The timed run was then begun by switching in the pre-weighed drying chamber.

A given run was continued for 30 to 80 min., depending on temperature and oxygen concentration, until sufficient water had been collected to allow reasonably precise rate determination. During this time, the pertinent system variables were monitored; if any appreciable drift occurred, the run was discontinued and discarded. An acceptable run was terminated by valving off the weighed drier. Samples were taken of the steady state gas phase and were analyzed by gas chromatography (Linde 13-X molecular sieve at 100°C. column temperature) (*6*). Weight of water formed, bulk gas composition, temperature and pressure differences, flowing gas velocity, and bulk temperature constituted the data for a given run.

Some nitrogen (a maximum of 16%) was always detected in the final gas samples. Presumably air was either ingested

Table 1. Reaction Rate Data

Run	$\mathcal{R}^*(\times 10^7)$ moles (cc.)(sec.)	$(C_A)_b(\times 10^7)$ moles/cc.	Equilibrium gas mole fractions† $(x_A)_b$	$(x_D)_b$	T_b, °C.	Measured differences between cylinder centers ΔT, °C.	ΔP, cm. oil
20-1	4.92	4.41	0.0093	0.0074	19.9	6.3	0.02
20-2	8.12	7.54	0.0159	0.0215	20.3	10.1	0.08
20-21	10.74	10.20	0.0215	0.0832	20.5	13.2	0.10
20-3	15.11	13.67	0.0288	0.0750	19.8	19.3	0.25
20-4	25.1	23.2	0.0489	0.1634	20.2	33.4	0.18
30-1	8.27	6.85	0.0152	0.0458	30.4	7.8	0.04
30-2	10.61	8.93	0.0195	0.0526	30.0	11.7	0.02
30-3	18.78	14.23	0.0313	0.109	30.1	20.1	0.06
30-31	12.79	9.18	0.0200	0.050	30.0	13.0	0.07
30-4	26.8	19.84	0.0434	0.101	30.7	30.0	0.06
50-1	5.85	3.03	0.0070	0.0279	48.4	5.7	0.02
50-2	11.47	6.58	0.0152	0.0503	47.9	11.6	0.05
50-3	18.34	9.74	0.0225	0.1027	48.1	17.4	0.09
50-41	32.7	19.04	0.0390	0.0599	48.0	32.2	0.10
60-1	8.94	3.69	0.0088	0.0530	58.5	7.2	0.04
60-2	12.80	4.71	0.0124	0.0207	58.7	11.1	0.05
60-3	21.3	8.83	0.0209	0.1195	58.8	17.4	0.09
60-4	28.9	11.60	0.0277	0.0767	58.6	26.6	0.09
50-4	21.1	11.53	0.0264	0.0656	48.3	20.6	0.04

† Based on dry stream composition.

during evacuation or was drawn in continuously around the diaphragm during the suction phase of the pump cycle. The amount of water which could have been drawn in with the air, assuming 100% relative humidity, was less than 3% of the total water collected in the worst (16% nitrogen) case. The leakage rate was too slow to be detected in the form of drift during a run, so that the only correction required was in the effective diffusivity used later to predict the effectiveness factor. It was assumed that nitrogen merely displaced hydrogen, and therefore had no effect on the hypothesized kinetics.

The data for a representative group of runs are given in Table 1. The rates of these and other runs are plotted vs. bulk oxygen concentration $(C_A)_b$ in Figure 3 at the four temperature levels investigated. A cross plot of rates vs. temperature at constant $(C_A)_b$ is shown in Figure 4.

Thermal Conductivity Determination

The effective thermal conductivity of the catalyst pellets was calculated from thermal diffusivity data obtained with air in the pore space. The apparatus is described in detail elsewhere (*6, 9*).

Four pellets from the same batch used in the rate runs were drilled axially and glued end to end as in the catalyst assembly. A butt-welded copper constantan thermocouple was inserted in the axial hole with its junction near the center of the pellet cylinder. The latter was mounted in a holder which could be moved rapidly between a hot air bath and a high velocity cold air stream.

The catalyst cylinder was brought to a steady temperature in the bath and then injected into the transverse cold air stream. The decline of the center temperature was recorded as a function of time as it dropped from the initial (bath) temperature to the final (air stream) temperature. The reduced temperature curves corresponded very closely with the appropriate theoretical curve for heat loss from an infinite circular cylinder with equivalent boundary condition (*12*).

The thermal diffusivity thus obtained and literature values for volumetric heat capacities were used to calculate the thermal conductivity of the catalyst pellets in air. The value of K_e^o obtained was $(3.5 \pm 0.1) \times 10^{-4}$ cal./(sec.) (cm.) (°C.), which agrees with a value reported by Mischke and Smith (*8*) for a similar material.

Effective Diffusivity Determination

Weisz' (*17*) simplification of the Wicke-Kallenback (*19*) procedure was used to determine the effective diffusivity of the catalyst. The gases used were hydrogen and oxygen. The samples were single pellets from the same batch as used in the reaction rate determination. The runs were made at essentially the same pressure as the reaction rate runs.

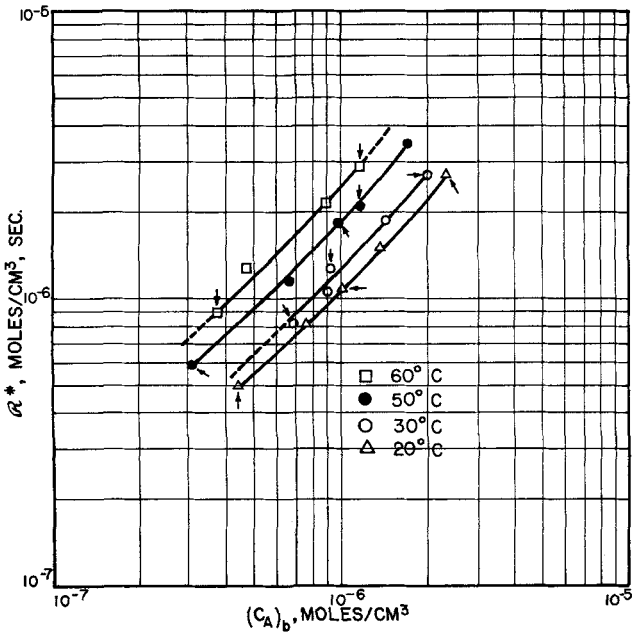

Fig. 3. Observed reaction rate vs. oxygen concentration at film surface.

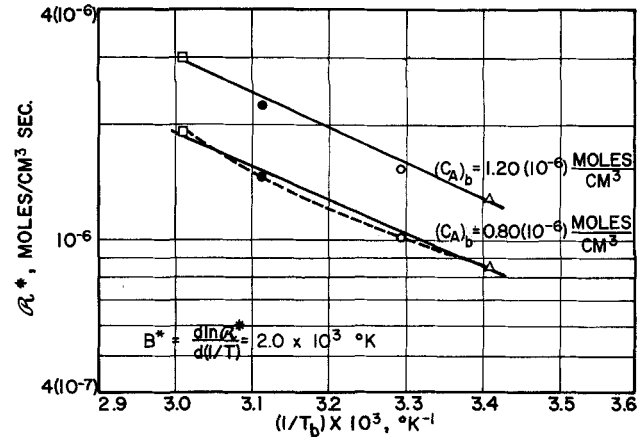

Fig. 4. Observed reaction rate vs. reciprocal surface temperature.

It was assumed that only the macropore system contributed to the steady state diffusivity, and that the diffusion was Fickian. Integration of the appropriate molar flux equation yields (*17*).

$$N_A = -\frac{c\, D_{AB}^{EFF}}{\omega L} \ln \left[\frac{1 - \omega}{1 - x_A \omega} \right] \qquad (1)$$

where $\omega = 1 + N_B/N_A$ and x_A in this case is the measured mole fraction of oxygen on the hydrogen-rich end of the porous sample.

According to Scott and Dullien (*13*) and Watson et al. (*16*), the molar fluxes for this system are related by

$$\frac{N_B}{N_A} = -\left(\frac{M_A}{M_B}\right)^{1/2}$$

regardless of the mode of diffusion which occurs. With this hypothesis, Equation (1) was used with the experimental x_A to obtain $D_{AB}^{EFF} = 0.115 \pm 0.004$ sq. cm./sec. at 1 atm. and at 26.5°C.

The ratio D_{AB}^{EFF}/D_{AB} is 0.137 for the catalyst used in this study, and should be a geometric factor characteristic of the porous medium. Wakao and Smith (*15*) suggest that this effectiveness ratio should be approximately the square of the macrovoid fraction for Fickian diffusion. $(\epsilon_{MACRO})^2$ is in fact 0.12 for the catalyst if the 120 Å. lower limit on the pore size distribution data is used. This agreement supports the assumption of Fickian diffusion in the macropore system.

THEORETICAL DEVELOPMENT

The Mathematical Model

The physical system was idealized as an infinitely long constant diameter cylinder of homogeneous isotropic porous catalyst material. The effect of the thermocouple present in the center of the actual cylinder was ignored, based on the diameter ratio of 16:1. The conditions at the surface of the cylinder were assumed to be such that angular variation of concentration, etc., could be ignored both on the surface and inside the cylinder. The local reaction rate inside the cylinder was taken to be

$$\mathcal{R} = Ae^{-B/T}(C_A)^n \qquad (2)$$

where B is the ratio of activation energy to the gas constant. C_A and T are the local macropore values of oxygen concentration and temperature. A, B, and n are assumed to be constant, which implies a micropore effectiveness factor of unity (discussed below). The effects of hydrogen and water concentration on the rate were ignored a priori.

The mass and heat transfer inside the porous material were assumed to be governed by Fick's and Fourier's laws, respectively, with temperature- and concentration-independent effective transport coefficients. Based on experimental evidence, the pressure rise produced by bulk flow was neglected, as was the heat transported by bulk flow and diffusion (6).

The development to follow parallels the work of Weisz and Hicks (18), differing only in that cylindrical rather than spherical geometry was used, the boundary condition at the surface was modified to account for film resistance to heat and mass transfer, a stoichiometry which produced a steady state bulk flow was necessarily employed, and a somewhat different numerical procedure was used to obtain the solutions.

With these assumptions the continuity equation for A (oxygen) and the energy equation are (at steady state)

$$\frac{1}{r}\frac{d}{dr}\left[r\,N_A)_r\right] = -\,\mathcal{R} \tag{3}$$

and

$$\frac{1}{r}\frac{d}{dr}\left[rq_r\right] = +\,(-\Delta H_A)\,\mathcal{R} \tag{4}$$

The fluxes are given by the following equations, which define the effective transport coefficients:

$$N_A)_r = -\,C\,D_{Am}^{EFF}\frac{dx_A}{dr} + x_A \sum_i N_i)_r \tag{5}$$

$$q_r = -\,K_e\frac{dT}{dr} \tag{6}$$

For the stoichiometry of the hydrogen-oxygen reaction, $\sum_i N_i)_r$ is just $+\,N_A)_r$, so that Equations (3) and (4) become

$$\frac{1}{r}\frac{d}{dr}\left(\frac{r\,C\,D_{Am}^{EFF}}{1-x_A}\frac{dx_A}{dr}\right) = \mathcal{R} \tag{7}$$

$$\frac{1}{r}\frac{d}{dr}\left(rK_e\frac{dT}{dr}\right) = -\,(-\Delta H_A)\mathcal{R} \tag{8}$$

When the assumptions of constant pressure, ideal gas mixture, and constant transport coefficients are invoked, these equations, combined with the rate expression [Equation (2)], reduce to

$$\frac{1}{r}\frac{d}{dr}\left(\frac{r}{(1-x_A)T}\frac{dx_A}{dr}\right) = \frac{1}{(C)_b\,T_b\,D_{Am}^{EFF}}\,Ae^{-B/T}(Cx_A)^n \tag{9}$$

$$\frac{1}{r}\frac{d}{dr}\left(r\frac{dT}{dr}\right) = -\frac{(-\Delta H_A)}{K_e}\,Ae^{-B/T}(Cx_A)^n \tag{10}$$

Dimensionless variables are defined based on the pellet radius R and bulk gas conditions. These variables and the associated dimensionless parameters are

$$\xi = \frac{r}{R};\quad \psi = \frac{x_A}{(x_A)_b}\quad \phi = \frac{T}{T_b}$$

$$\alpha^2 = \frac{R^2\,Ae^{-B/T_b}}{D_{Am}^{EFF}}\,(C_A)_b{}^{n-1};\quad \beta = \frac{B}{T_b};$$

$$\lambda = \frac{(-\Delta H_A)D_{Am}^{EFF}(C_A)_b}{K_e\,T_b}$$

The results of rewriting Equations (9) and (10) in terms of dimensionless quantities are

$$\frac{1}{\xi}\frac{d}{d\xi}\left(\frac{\xi}{(1-(x_A)_b\,\psi)\,\phi}\frac{d\psi}{d\xi}\right) = \alpha^2\,e^{\beta\left(1-\frac{1}{\phi}\right)}\left(\frac{\psi}{\phi}\right)^n \tag{11}$$

$$\frac{1}{\xi}\frac{d}{d\xi}\left(\xi\frac{d\phi}{d\xi}\right) = -\,\lambda\,\alpha^2\,e^{\beta\left(1-\frac{1}{\phi}\right)}\left(\frac{\psi}{\phi}\right)^n \tag{12}$$

The dimensionless boundary conditions appropriate to the idealized situation are

$$\frac{d\psi}{d\xi} = \frac{d\phi}{d\xi} = 0 \quad \text{at} \quad \xi = 0 \tag{13}$$

$$\left.\begin{aligned}\frac{1}{N_M(1-(x_A)_b)\,\psi}\frac{d\psi}{d\xi} + \psi &= 1\\ \frac{1}{N_H}\frac{d\phi}{d\psi} + \phi &= 1\end{aligned}\right\} \quad \text{at} \quad \xi = 1 \tag{15}$$

where the dimensionless transport numbers are given by

$$N_M = \frac{k_G\,R}{(1-(x_A)_b)C_b\,D_{Am}^{EFF}} \quad \text{and} \quad N_H = \frac{h\,R}{K_e}$$

The conditions in Equations (14) and (15) are obtained by equating the internal and external (film) fluxes at the pellet surface. k_G and h are the external film mass and heat transfer coefficients, respectively.

Equations (11) and (12) were integrated numerically with the indicated boundary conditions for various values of the parameters α, β, λ, n, $(x_A)_b$, N_M, and N_H. The Rice University high-speed digital computer was used to perform the calculations. The details of the numerical procedure, the computer program, and a complete set of parametric plots are reported elsewhere (6).

If Equation (11) is multiplied by λ and added to Equation (12), the following relation results after an integration and the use of the boundary condition in Equation (13):

$$\frac{\lambda}{(1-(x_A)_b\,\psi)\phi}\frac{d\psi}{d\xi} + \frac{d\phi}{d\xi} = 0,\quad 0 \le \xi \le 1 \tag{16}$$

This result can be integrated again and combined with the conditions of Equations (14) and (15) to yield a relation of the form

$$\psi = \psi[\phi, \phi(1), \lambda, \ldots.] \tag{17}$$

where $\phi(1)$ is the unknown dimensionless temperature at $\xi = 1$. Equation (17) could have been used to eliminate the dimensionless concentration from Equation (12), thus decoupling the heat and mass balances. However, the unknown $\phi(1)$ would have appeared in the rate term, and certain limiting cases would have been ill-behaved.

Instead, a straightforward iteration procedure was used to solve Equations (11) and (12) simultaneously. The equations and boundary conditions were finite-differenced on a grid $\xi = k\Delta\xi$. For given values of α, n, $(x_A)_b$, N_M, N_H, and for $\lambda = 0$, the resulting set of simultaneous equations for the grid point values ψ_k was solved by iteration. This gave the concentration profile for the equivalent isothermal problem, which was used as the initial trial profile for the actual problem.

The trial ψ_k were used in the finite-differenced form of Equation (12) on the same grid. The set of simultaneous equations for the ϕ_k was also solved by iteration. This yielded a first approximation to a temperature profile, which was then used to improve the coefficients in the

equation for the ψ_k. The latter were solved again to give a second approximation concentration profile, and so forth. The process was terminated after the profiles had stabilized to four significant figures over the entire range. For the range of parameters of interest in this study, a forty grid-point mesh gave adequate accuracy, as determined by the usual mesh-size halving procedure. Both iteration and truncation errors were well below the level required by the analysis of the data, which was only accurate to two figures.

The effectiveness (or utilization) factor η is defined in the usual way as the ratio of the average rate of reaction observed to the rate which would be observed if the bulk gas temperature and concentration existed everywhere inside the catalyst cylinder. By this definition

$$\mathcal{R}^* = \eta\, A e^{-B/T_b} (C_A)_b^{\,n} \tag{18}$$

which can be used in reactor design calculations once η and the constants are known.

In terms of the variables and parameters defined earlier

$$\eta = \frac{2}{\alpha^2 (1 - (x_A)_b\, \psi)\phi} \left.\frac{d\psi}{d\xi}\right]_{\xi=1} \tag{19}$$

η is thus obtainable from the numerical solutions for ψ and ϕ for given α, β, λ, N_H, N_M, n, and $(x_A)_b$.

Figure 5 shows a typical set of computed curves plotted in the manner proposed by Weisz and Hicks (*18*). This form was employed since $\eta\alpha^2$ depends only on observable quantities. From the definition of α and Equation (18)

$$\eta\alpha^2 = \frac{\mathcal{R}^*\, R^2}{D_{Am}^{EFF}\, (C_A)_b} \tag{20}$$

All of the quantities on the right side of Equation (20) were in fact measured in this work.

The reduction of the experimental data was simplified by the relative insensitivity of η to changes in certain parameters within the range of the experimental data. Average values for N_M of 22 (range 19.6 to 24.6), N_H of 11 (8.7 to 12.8), $(x_A)_b$ of 0.02 (0.0070 to 0.0489), and an n of 1 were used in computing the curves required in the following discussion.

The values of η calculated in this work are 20 to 30% below those reported by Weisz and Hicks (*18*) for the same range of α, β, and λ. The difference gives a quantitative measure of the importance of the factors mentioned earlier, namely, geometry, boundary conditions, and the stoichiometry of the reaction, as well as of a somewhat different definition of molar flux [Equation (5)] used here.

REDUCTION OF THE EXPERIMENTAL DATA

Determination of the unknown constants A, B, and n in the proposed rate of Equation (2) had to be carried out simultaneously with the calculation of η for the individual runs. The runs selected for evaluation of A, B, and n are indicated by the small arrows in Figure 3.

The only parameter (other than N_M, N_N, and $(x_A)_b$, as noted above) which could be calculated independently was λ. The latter contains D_{AM}^{EFF} and K_e, which had to be computed from D_{AB}^{EFF} and K_e^o, respectively. The correlation of Godbee (*4*) was used to convert the thermal conductivity in air to that in hydrogen. The uncertainty in this correction lies mainly in the estimation of a characteristic pore diameter and an accommodation coefficient. The macropore peak at 900 Å. was used along with literature values for hydrogen accommodation coefficient to yield a corrected K_e of $(5.4 \pm 0.5) \times 10^{-4}$ cal./(sec.)(cm.)(°C.). The uncertainty was large enough to discourage further attempts at temperature and concentration corrections.

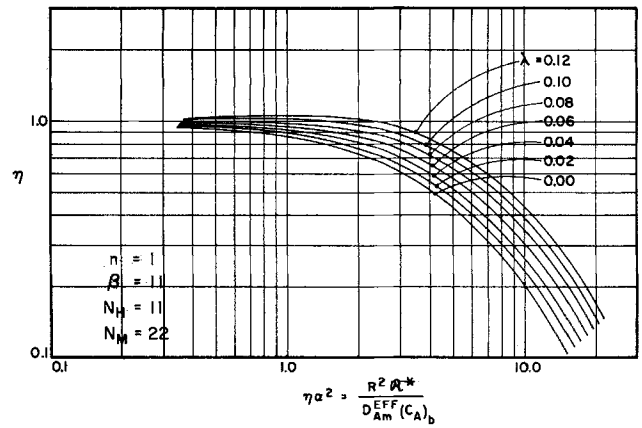

Fig. 5. Effectiveness factor vs. $\eta\alpha^2$ for various λ at average system values of β, N_H, N_M, and $n = 1$.

The effective mixture diffusivity for oxygen in the macropore system was calculated from an equation suggested by Bird et al. (*1*):

$$\frac{D_{Am}^{EFF}}{D_{AB}^{EFF}} = \frac{D_{Am}}{D_{AB}} = \frac{N_A - x_A \sum_i^i N_i}{\sum_i \frac{D_{AB}}{D_{Ai}} (x_i N_A - x_A N_i)} \tag{21}$$

If the nitrogen flux is ignored ($N_D = 0$) and the specific stoichiometric restrictions are introduced $\left(N_A = \frac{N_B}{2} = -\frac{N_C}{2}\right)$

$$\frac{D_{Am}^{EFF}}{D_{AB}^{EFF}} = \frac{1 - x_A}{\left(x_B - \frac{x_A}{2}\right) + \frac{D_{AB}}{D_{AC}}\left(x_C + \frac{x_A}{2}\right) + \frac{D_{AB}}{D_{AD}} x_D} \tag{22}$$

In the actual calculation of D_{AM}^{EFF}, bulk (dry) mole fractions were used. The results were quite insensitive to extent of reaction (x_C) in the range used in this study, so that variation with concentration inside the pellet could be ignored. D_{AB}/D_{AC} and D_{AB}/D_{AD} were assumed to have constant values of 3.4 and 3.7, respectively. D_{AB}^{EFF} was taken to be proportional to $(T_B)^{0.8}$; no correction for the effect of internal temperature rise on D_{AB}^{EFF} was attempted. The resulting D_{AM}^{EFF} are given in column 2 of Table 2.

$\eta\alpha^2$ and λ could now be calculated from Equation (20) and the definition

$$\lambda = \frac{(-\Delta H_A)\, D_{Am}^{EFF} (C_A)_b}{K_e\, T_b} \tag{23}$$

The values are shown in columns 3 and 4 of Table 2.

Preliminary estimates of the size of B and n were first obtained from the apparent activation energy (Figure 4) and the slope of $\mathcal{R}^*$ vs. $(C_A)_b$ (Figure 3), along with the following analysis.

From Equation (18)

$$\left.\frac{\partial \ln \mathcal{R}^*}{\partial \ln (C_A)_b}\right|_{T_b} = n + \frac{\partial \ln \eta}{\partial \ln (C_A)_b} \tag{24}$$

Since η is a sensitive function of only two parameters which depend on $(C_A)_b$, namely, α and λ

TABLE 2. CALCULATED RESULTS

Run	D_{AM}^{EFF}, sq. cm./sec.	$\frac{\mathcal{R}^* R^2}{(C_A)_b D_{AM}^{EFF}}$	λ	η	α^2	$Ae^{-\beta}$, (mole/cc.)$^{0.2}$ (sec.$^{-1}$)	Calc. ΔT, °C.	Obs. ΔT, °C.	Isothermal η
20-1	0.105	2.4	0.034	0.74	3.3	8.2×10^{-2}	6.1	6.3	0.67
20-21	0.086	2.8	0.064	0.80	3.5	8.3	12.9	13.2	0.62
20-4	0.071	3.4	0.120	0.89	3.9	9.1	30.5	33.4	0.56
						Avg: 8.5×10^{-2}	(8.0×10^{-2})		
30-1	0.102	2.7	0.049	0.75	3.6	9.5×10^{-2}	10.3	7.8	0.63
30-3	0.087	3.5	0.087	0.79	4.4	11.6	22.4	20.1	0.55
30-4	0.087	3.5	0.122	0.90	3.9	11.0	32.6	30.0	0.55
						Avg: 10.7×10^{-2}	(10.8×10^{-2})		
50-1	0.111	4.0	0.022	0.56	7.1	17×10^{-2}	5.8	5.7	0.51
50-3	0.099	4.3	0.063	0.64	6.8	19	18.5	17.4	0.49
50-4	0.106	3.9	0.081	0.73	5.4	16	23.4	20.6	0.52
						Avg: 17.3×10^{-2}	(18.8×10^{-2})		
60-1	0.120	4.6	0.029	0.53	8.6	24×10^{-2}	8.3	7.2	0.48
60-4	0.111	5.1	0.083	0.63	8.1	25	25.9	26.6	0.42
						Avg: 24.5×10^{-2}	(23.5×10^{-2})		

Final constants: B = 2,750°K. (E_A = 5.5 kcal.). A = 8.0 × 10^2 (moles/cc.)$^{0.2}$(sec.$^{-1}$). n = 0.8.

$$\frac{\partial \ln \eta}{\partial \ln (C_A)_b} \doteq \frac{\partial \ln \eta}{\partial \lambda} \frac{\partial \lambda}{\partial \ln (C_A)_b} + \frac{\partial \ln \eta}{\partial \ln \alpha} \frac{\partial \ln \alpha}{\partial \ln (C_A)_b} \tag{25}$$

From the definitions of the parameters

$$\frac{\partial \ln \eta}{\partial \ln (C_A)_b} \doteq \lambda \frac{\partial \ln \eta}{\partial \lambda} + \frac{n-1}{2} \frac{\partial \ln \eta}{\partial \ln \alpha} \tag{26}$$

If average values of the derivatives in the observed range of $\eta\alpha^2$ are used

$$\left.\frac{\partial \ln \mathcal{R}^*}{\partial \ln (C_A)_b}\right|_{T_b} \doteq n + 3.5\,\lambda + 0.35\,(1-n) \tag{27}$$

This equation indicates the extent to which the apparent order can differ from the actual order for nonisothermal systems, even if the actual order is unity. The approximate n obtained from Equation (27) and Figure 3 is 0.75.

The apparent value of B (activation energy divided by gas constant) can also be obtained from Equation (18):

$$B^* = -\left.\frac{\partial \ln \mathcal{R}^*}{\partial\, 1/T_b}\right|_{(C_A)_b} = B - \left.\frac{\partial \ln \eta}{\partial\, 1/T_b}\right|_{(C_A)_b} \tag{28}$$

By expanding the second term

$$\frac{\partial \ln \eta}{\partial\, 1/T_b} = \frac{\partial \ln \eta}{\partial \ln \alpha} \frac{\partial \ln \alpha}{\partial\, 1/T_b} + \frac{\partial \ln \eta}{\partial \beta} \frac{\partial \beta}{\partial\, 1/T_b} + \frac{\partial \ln \eta}{\partial \lambda} \frac{\partial \lambda}{\partial\, 1/T_b} \tag{29}$$

$$= -\frac{B}{2} \frac{\partial \ln \eta}{\partial \ln \alpha} + B \frac{\partial \ln \eta}{\partial \beta} + (\lambda T_b) \frac{\partial \ln \eta}{\partial \lambda} \tag{30}$$

from the definitions of α, β, and λ. Only the first term on the right side of Equation (30) is significant in the range of $\eta\alpha^2$ encountered. An average value for $-(\partial \ln \eta/\partial \ln \alpha)$ of 0.7 yields an approximate B of 3.0 × 10^3 °K.

Once B and n were set, the appropriate graph of η vs. $\eta\alpha^2$ could be used to obtain η and α^2, since $\eta\alpha^2$ was known. These results are given in the fifth and sixth columns of Table 2.

$Ae^{-\beta}$ could then be obtained from the definition of α. The value of n was then corrected to give the least deviation among the values of $Ae^{-\beta}$ for the runs at each temperature level. Finally, the corrected averages of $Ae^{-\beta}$ were plotted vs. $1/T_b$ to obtain a corrected value of B. The best values were n = 0.8, B = 2.75 × 10^3 °K., and A = 8.0 × 10^2 (moles/cc.)$^{0.2}$(sec.)$^{-1}$. The resulting $Ae^{-\beta}$ for the various temperatures are shown in parentheses next to the experimental averages in Table 2.

Finally, the appropriate solutions for ϕ vs. ξ were used to determine $\phi(0)$, the dimensionless temperature at the pellet center. The calculated temperature rise was then $(\phi(0) - 1)T_b$, which is shown in the eighth column of Table 2 for the runs used to compute the parameters.

DISCUSSION

As stated earlier, only the macroeffectiveness factor was taken into account in this treatment, the microeffectiveness factor having been assumed to be unity. The validity of the later assumption can be tested with the computed curves of Mingle and Smith (7). An average micropore diameter of 30 Å. and an average micropore length of 0.01 cm. were used to compute the micro Thiele modulus defined by the latter authors. The value of 10^{-3} obtained (which is conservatively large) could be an order of magnitude larger and still predict a value of unity for the microeffectiveness factor.

It can be seen from Table 2 that the rate Equation (2) gives generally consistent results. The average deviation, on the order of ± 10%, is no worse than the scatter of the experimental data. The maximum experimental error in $\eta\alpha^2$ was estimated to be ± 12% at the lowest concentration level (6).

The activation energy calculated from B is 5.5 cal./(mole)(°K.), which is somewhat smaller than the value of (6.5 cal./(mole)(°K.) reported by Trotter (*14*) for the same reaction on a similar material. Both B and n are in good agreement with the more recent work of Maymo and Smith (5).

The validity of the quasihomogeneous transport theory used is supported by the relatively close agreement of predicted and observed temperature differences (Table 2). The predicted values range from 60 to 90% of the maximum temperature rise which could exist for the given conditions. The latter number, equivalent to the Damköhler (*3, 11*) ΔT for linear kinetics and equimolar stoichiometry, is obtained from Equation (16) and the boundary conditions used, Equations (14) and (15). If Equation (16) is to hold and if no discontinuities are to exist at ξ = 1, it must follow that

$$\lambda N_M [1 - \psi(1)] = N_H [\phi(1) - 1] \tag{31}$$

For small $(x_A)_b$ Equation (16) can be integrated approximately to yield

$$2\lambda\psi + \phi^2 = \text{const.} = 2\lambda\psi(1) + \phi^2(1) \qquad (32)$$

The maximum obtainable ϕ occurs at $\xi = 0$ when ψ is vanishingly small. Thus, when $\psi(1)$ is eliminated by using Equation (31)

$$\phi^2_{\max} = (1 + \Delta)^2 + 2\lambda - \frac{2N_H}{N_M}\Delta \qquad (33)$$

where $\Delta = \phi(1) - 1$, the dimensionless film temperature rise. For the parameter values encountered experimentally $(2N_H/N_M)$ is approximately unity. The temperature rise is then given by

$$(\Delta T)_{\max} = T_b\{[(1 + \Delta)^2 + 2\lambda - \Delta]^{1/2} - 1\} \qquad (34)$$

or, since Δ and λ are much less than 1,

$$(\Delta T)_{\max} \cong T_b\left(\lambda + \frac{\Delta}{2}\right) \qquad (35)$$

Since the dimensionless film temperature rise Δ was of the same order as λ, this correction to the Damköhler relation was not negligible.

The last column in Table 2 is the effectiveness factor which would be calculated if thermal effects were ignored. Even for the relatively mild conditions encountered in this experiment, the isothermal approximation was as much as 40% below the nonisothermal value.

ACKNOWLEDGMENT

The authors would like to thank Engelhard Industries for the catalyst; A. B. Stiles of Du Pont for surface area and pore volume measurements; Humble Production Research Labs for permeability measurements; and Monsanto Chemical Company and Pan American Petroleum Corporation for financial support of the project and a grant to F. W. Miller.

NOTATION

A = frequency factor in the rate expression [Equation (2)], (moles/cc.)$^{1-n}$(sec.)$^{-1}$
B = activation energy/gas constant, °K.
B^* = apparent activation energy/gas constant, °K. (Figure 4)
C = local gas phase concentration, moles/cc.
C_A = local oxygen concentration, moles/cc.
C_B = local hydrogen concentration, moles/cc.
$(C_A)_b$ = bulk (circulating) gas oxygen concentration, moles/cc.
D = catalyst pellet diameter (⅜ in.)
D_{ij} = binary diffusivity, sq.cm./sec.
D^{EFF}_{AB} = effective diffusivity, hydrogen-oxygen, in the porous catalyst, sq.cm./sec.
D^{EFF}_{Am} = effective diffusivity, oxygen in reaction mixture, in the porous catalyst, sq.cm./sec.
$(-\Delta H_A)$ = average heat of reaction per mole oxygen converted, cal./g.-mole
h = film heat transfer coefficient, cal./(sq.cm.)(sec.)(°K.)
k_G = film mass transfer coefficient, moles/(sq.cm.)(sec.)
K_E = effective thermal conductivity of porous catalyst in hydrogen atmospheres, cal./(cm.)(sec.)(°K.)
K_E^o = effective thermal conductivity of porous catalyst in air, cal./(cm.)(sec.)(°K.)
k = index on the finite-difference grid $\xi = k\Delta\xi$
L = length of catalyst cylinder, cm.
M_i = molecular weight of i
n = order for oxygen in the reaction rate expression [Equation (2)]
N_A = oxygen molar flux, moles/(sq.cm.)(sec.)
N_B = hydrogen molar flux, moles/(sq.cm.)(sec.)
N_C = water vapor molar flux, moles/(sq.cm.)(sec.)
N_D = nitrogen molar flux, moles/(sq.cm.)(sec.)
N_H = dimensionless heat transfer number, defined after Equation (5)
N_M = dimensionless mass transfer number, defined after Equation (5)
r = radial position, cm.
R = catalyst cylinder outer radius, cm.
$\mathcal{R}$ = local rate of oxygen conversion, moles oxygen/(volume catalyst)(time)
$\mathcal{R}^*$ = measured average rate of oxygen conversion, moles oxygen/(volume catalyst)(time)
T = local gas and solid phase temperature, °K.
T_b = bulk (circulating) gas phase temperature, °K.
x_A = local oxygen mole fraction
$(x_A)_b$ = bulk gas phase oxygen mole fraction

Greek Letters

α = dimensionless parameter defined after Equation (10)
β = dimensionless parameter defined after Equation (10)
Δ = dimensionless film temperature rise
ϵ = void fraction
η = effectiveness (utilization) factor, defined by Equations (18) and (19)
λ = dimensionless parameter, defined after Equation (10)
ξ = dimensionless radial position, r/R
ϕ = dimensionless temperature, T/T_b
ψ = normalized oxygen mole fraction $x_A/(x_A)_b$

Subscripts

A = oxygen
B = hydrogen
C = water
D = nitrogen
b = bulk (circulating) gas phase
m = mixture
r = radial component
(1) = evaluated at $\xi = 1$, inside the surface film
(0) = evaluated at $\xi = 0$, pellet center

LITERATURE CITED

1. Bird, R. B., W. E. Stewart, and E. N. Lightfoot, "Transport Phenomena," Wiley, New York (1960).
2. Carberry, J. J., *A.I.Ch.E. J.*, **7**, 350 (1961).
3. Damköhler, G., *Z. Phys. Chem.*, **A193**, 16 (1943).
4. Godbee, H. W., Oak Ridge Natl. Lab., private communication.
5. Maymo, J. A., and J. M. Smith, *A.I.Ch.E. J.*, **12**, 845 (1966).
6. Miller, F. W., Ph.D. thesis, Rice Univ., Houston, Tex. (1964).
7. Mingle, J. O., and J. M. Smith, *A.I.Ch.E. J.*, **7**, 243 (1961).
8. Mischke, R. A., and J. M. Smith, *Ind. Eng. Chem. Fundamentals*, **1**, 288 (1960).
9. Park, E. L., M.S. thesis, Rice Univ., Houston, Tex. (1962).
10. Peterson, E. E., "Chemical Reaction Analysis," Prentice-Hall, Englewood Cliffs, N. J. (1965).
11. Prater, C. D., *Chem. Eng. Sci.*, **8**, 284 (1958).
12. Schneider, P. J., "Temperature Response Charts," Wiley, New York (1962).
13. Scott, D. S., and F. A. Dullien, *A.I.Ch.E. J.*, **8**, 113 (1962).
14. Trotter, I. P., Ph.D. thesis, Princeton Univ., N. J. (1958).
15. Wakao, Noriaki, and J. M. Smith, *Chem. Eng. Sci.*, **17**, 825 (1962).
16. Watson, G. M., R. B. Evans III, and E. A. Mason, *J. Chem. Phys.*, **35**, 2076 (1961).
17. Weisz, P. B., *Z. Phys. Chem.*, **11**, 1 (1957).
18. ———, and J. S. Hicks, *Chem. Eng. Sci.*, **17**, 265 (1962).
19. Wicke, E., and R. Kallenback, *Kolloid Z.*, **97**, 135 (1941).

Manuscript received March 12, 1965; revision received May 17, 1966; paper accepted May 20, 1966. Paper presented at A.I.Ch.E. San Francisco meeting.